

AD-A186 371

NUMERICAL CALCULATION OF APPENDAGE--FLAT PLATE JUNCTION 1/1

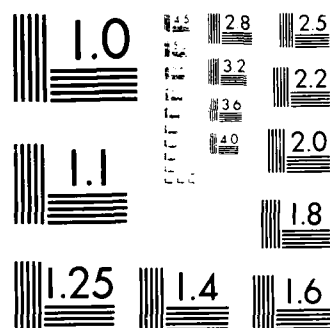
FLOW(U) DAVID W TAYLOR NAVAL SHIP RESEARCH AND

DEVELOPMENT CENTER BETHESDA MD R W BURKE SEP 87

F/G 28/4

NL

UNCLASSIFIED



MICROCOPY RESOLUTION TEST CHART
NATIONAL BUREAU OF STANDARDS-1963-A

David W. Taylor Naval Ship Research and Development Center

Bethesda, MD 20084-5000

DTIC FILE COPY

12

DTNSRDC-87/002 September 1987

Ship Performance Department
Research and Development Report

AD-A186 371

**Numerical Calculation of
Appendage-Flat Plate
Junction Flow**

by
Roger W. Burke

DTIC
ELECTE
OCT 07 1987
S **D**
CSD

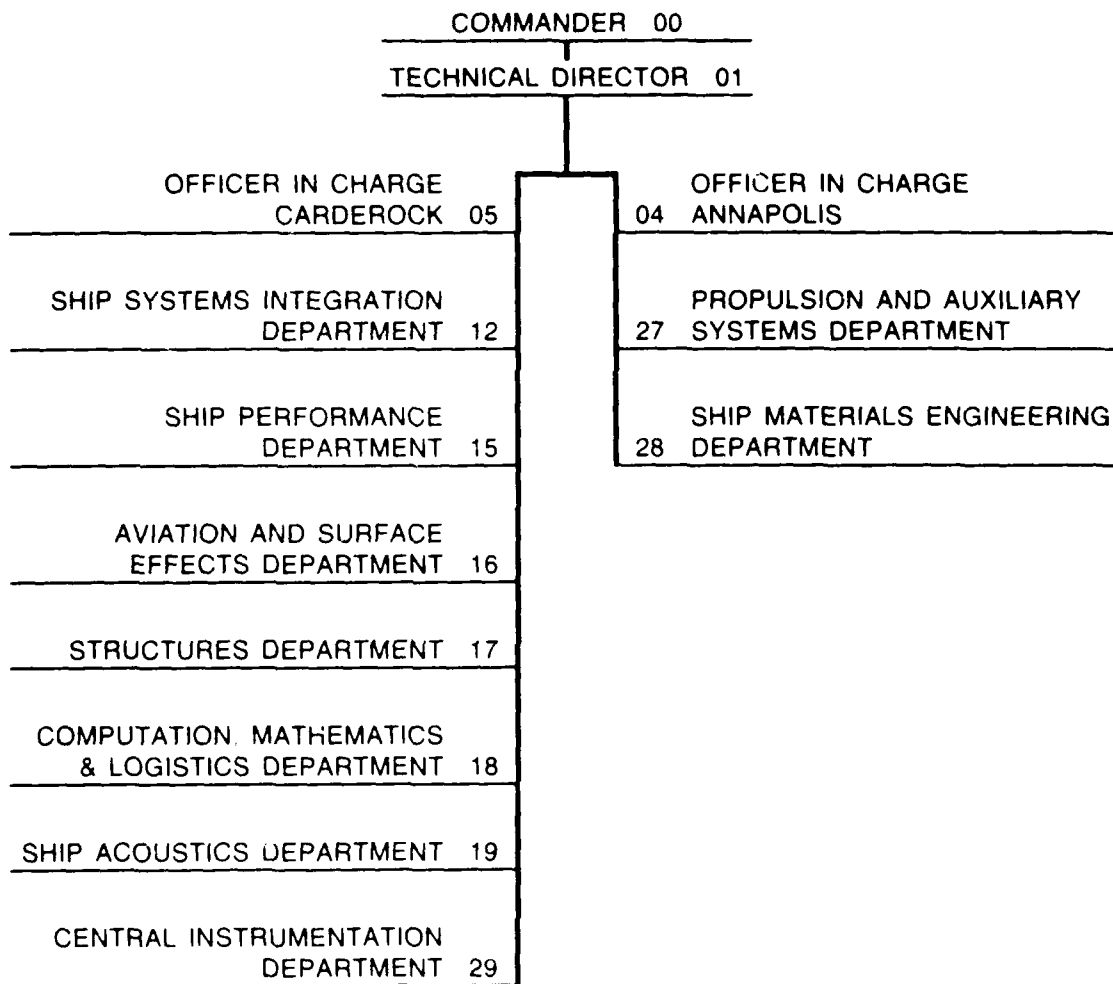
DTNSRDC-87/002 Numerical Calculation of Appendage-Flat Plate
Junction Flow



Approved for public release; distribution is unlimited.

87 10 2 155

MAJOR DTNSRDC TECHNICAL COMPONENTS



DESTRUCTION NOTICE — For **classified** documents, follow the procedures in DOD 5220.22M, Industrial Security Manual, Section II-9, or DOD 5200.1-R, Information Security Program Regulation, Chapter IX. For **unclassified**, limited documents, destroy by any method that will prevent disclosure of contents or reconstruction of the document.

AD-7186371

REPORT DOCUMENTATION PAGE

1a REPORT SECURITY CLASSIFICATION Unclassified		1b RESTRICTIVE MARKINGS	
2a SECURITY CLASSIFICATION AUTHORITY		3 DISTRIBUTION / AVAILABILITY OF REPORT APPROVED FOR PUBLIC RELEASE: DISTRIBUTION IS UNLIMITED.	
2b DECLASSIFICATION / DOWNGRADING SCHEDULE			
4 PERFORMING ORGANIZATION REPORT NUMBER(S) DTNSRDC-87 002		5 MONITORING ORGANIZATION REPORT NUMBER(S)	
6a NAME OF PERFORMING ORGANIZATION David W. Taylor Naval Ship R&D Center	6b OFFICE SYMBOL (If applicable) Code 1542	7a NAME OF MONITORING ORGANIZATION	
6c ADDRESS (City, State, and ZIP Code) Bethesda, MD 20084-5000		7b ADDRESS (City, State, and ZIP Code)	
8a NAME OF FUNDING / SPONSORING ORGANIZATION Naval Sea Systems Command	8b OFFICE SYMBOL (If applicable) Code 05R24	9 PROCUREMENT INSTRUMENT IDENTIFICATION NUMBER	
8c ADDRESS (City, State, and ZIP Code) Washington, DC 20362		10 SOURCE OF FUNDING NUMBERS	
		PROGRAM ELEMENT NO 61153N	PROJECT NO SR0230101
		TASK NO DN1780611	WORK UNIT ACCESSION NO DN1780611
11 TITLE (Include Security Classification) NUMERICAL CALCULATION OF APPENDAGE FLAT PLATE JUNCTION FLOW.			
12 PERSONAL AUTHOR(S) Burke, Roger W.			
13a TYPE OF REPORT Final	13b TIME COVERED FROM TO	14 DATE OF REPORT (Year, Month, Day) 1987 September	15 PAGE COUNT 37
16 SUPPLEMENTARY NOTATION			
17 COSATI CODES		18 SUBJECT TERMS (Continue on reverse if necessary and identify by block number)	
FIELD	GROUP	SUB-GROUP	
		Separated flow Three dimensional flow	
		Turbulence Computer simulation	
19 ABSTRACT (Continue on reverse if necessary and identify by block number)			
<p>A steady, incompressible, three-dimensional Reynolds equation solver was applied to the problem of flow past an appendage mounted on a flat plate. The code, called INS3D, was developed in a joint effort between NASA Ames Research Center and Rocketdyne. INS3D handles the pressure using a pseudo-compressibility approach to obtain a steady-state solution. A beam-warming approximate factorization scheme is used to discretize the equations. A Baldwin-Lomax type scheme was used to parameterize the shear stresses for the appendage-flat plate problem. Comparisons were made with wind tunnel experiments of Dickinson, conducted in the low turbulence wind tunnel at DTNSRDC. The observed and predicted pressure distributions on the flat plate agreed well, but the lateral extent of the horseshoe vortex was overpredicted compared to experimental data. Predicted mean and cross flow velocities exhibited all the essential features of the appendage-flat plate corner region, and showed good qualitative agreement with the experiments.</p>			
20 DISTRIBUTION / AVAILABILITY OF ABSTRACT <input type="checkbox"/> UNCLASSIFIED UNLIMITED <input type="checkbox"/> SAME AS RPT <input type="checkbox"/> DTIC USERS		21 ABSTRACT SECURITY CLASSIFICATION Unclassified	
22a NAME OF RESPONSIBLE INDIVIDUAL Thomas T. Huang		22b TELEPHONE (Include Area Code) (301) 227-1325	22c OFFICE SYMBOL Code 1542

UNCLASSIFIED

SECURITY CLASSIFICATION OF THIS PAGE

UNCLASSIFIED

SECURITY CLASSIFICATION OF THIS PAGE

CONTENTS

	Page
Abstract	1
Administrative Information	1
Introduction	1
Numerical Procedure	2
Governing Equations	2
Grid Generation	4
Boundary Conditions	4
Turbulence Model	5
Results and Discussion	7
Pressure Distribution	7
Oil Flow Visualization	7
Velocity	9
Plane $x = 0.18$	9
Plane $x = 0.75$	9
Plane $x = 1.5$	10
Summary and Conclusions	11
Acknowledgments	12
References	27

FIGURES

1. C grid used in numerical computations	13
2. Orientation of grid system	13
3. Experimental and numerical mean velocity profiles (u vs. z) for $x = -0.75$ and $y = 0$	14
4. Pressure distribution on flat plate near appendage	14
5. Velocity vectors in the symmetry plan $y = 0$, ahead of wing	15
6. Oil-film flow visualization on flat plate (Dickinson, 1986)	15
7. Numerical flow simulation on flat plate, $z = 0$	16
8. Numerical flow simulation, showing detailed streamlines at leading edge on flat plate $z = 0$	16
9. Experimental mean velocity contours at $x = 0.18$ (Dickinson, 1986)	17
10. Numerical mean velocity contours at $x = 0.18$	17
11. Experimental and numerical mean velocity profiles (u vs. z) at $x = 0.176$ and $y = 0.1471$	18
12. Experimental and numerical mean velocity profiles (u vs. z) at $x = 0.176$ and $y = 0.1716$	18
13. Experimental cross-flow vectors at $x = 0.18$ (Dickinson, 1986)	19



	Page
14. Numerical cross-flow velocity vectors at $x = 0.18$	19
15. Experimental mean velocity contours at $x = 0.75$ (Dickinson, 1986) . . .	20
16. Numerical mean velocity contours at $x = 0.75$	20
17. Experimental and numerical mean velocity profiles (u vs. z) for $x = 0.75$ and $y = 0.0588$	21
18. Experimental and numerical mean velocity profiles (u vs. z) for $x = 0.75$ and $y = 0.098$	21
19. Experimental and numerical mean velocity profiles (u vs. z) for $x = 0.75$ and $y = 0.245$	22
20. Experimental cross-flow velocity vectors at $x = 0.75$ (Dickinson, 1986)	22
21. Numerical cross-flow velocity vectors at $x = 0.75$	23
22. Experimental mean velocity contours at $x = 1.5$ (Dickinson, 1986)	23
23. Numerical mean velocity contours at $x = 1.5$	24
24. Experimental and numerical mean velocity profiles (u vs. z) for $x = 1.5$ and $y = 0.0245$	24
25. Experimental and numerical mean velocity profiles (u vs. z) for $x = 1.5$ and $y = 0.049$	25
26. Experimental and numerical mean velocity profiles (u vs. z) for $x = 1.5$ and $y = 0.2206$	25
27. Experimental cross-flow velocity vectors at $x = 1.5$ (Dickinson, 1986)	26
28. Numerical cross-flow velocity vectors at $x = 1.5$	26

ABSTRACT

A steady, incompressible, three-dimensional Reynolds equation solver was applied to the problem of flow past an appendage mounted on a flat plate. The Code, called INS3D, was developed in a joint effort between NASA Ames Research Center and Rocketdyne. INS3D handles the pressure using a pseudocompressibility approach to obtain a steady-state solution. A beam-warming approximate factorization scheme is used to discretize the equations. A Baldwin-Lomax type scheme is used to parameterize the shear stresses for the appendage-flat plate problem. Comparisons were made with wind tunnel experiments of Dr. S. Dickinson, which were conducted in the low turbulence wind tunnel at David Taylor Naval Ship Research and Development Center (DTNSRDC). The observed and predicted pressure distributions on the flat plate agree well, but the lateral extent of the horseshoe vortex is overpredicted compared to experimental data. Predicted mean and cross-flow velocities exhibit all the essential features of the appendage-flat plate corner region and show good qualitative agreement with the experiments.

ADMINISTRATIVE INFORMATION

The work described in this report was funded under the Naval Sea Systems Command (05R24) Special Focus Program on Ship and Submarine Appendage Drag and Wake Prediction, using Program Element 61153N, Task Area SR0230101, and DTNSRDC Work Units 1542-101 and 1542-106.

INTRODUCTION

Wing-body junction, or corner, flow occurs when an obstruction is placed within an approaching boundary layer. The resulting three-dimensional viscous flow occurs in many branches of fluid engineering such as the wing-fuselage juncture of aircraft, the blade-hub juncture of turbomachinery, and the hull-appendage juncture of ships.

The dominant feature of this wing-body junction flow is a horseshoe vortex system that is caused by the steep adverse pressure gradients set up just forward of the leading edge of the obstruction. As a result of these pressure gradients, the vorticity in the oncoming boundary layer wraps around the obstruction in a characteristic horseshoe shape, with each leg having the vorticity of opposite rotational sense. In the ship hull-appendage case, this horseshoe vortex may proceed downstream and impinge upon the propeller, thus affecting propeller performance. In addition to its effect on the propeller, the horseshoe vortex may also influence the drag of the ship.

Computation of the wing-body junction flow, with its associated large separated flow region, generally precludes the use of simplified flow equation techniques, such as the boundary layer approach. Instead, it becomes necessary to solve the complete set of Reynolds equations.

This study describes the application of a steady, incompressible, fully three-dimensional Reynolds-average Navier-Stokes solver to the wing-body junction problem. Specifically, the flow past an appendage mounted on a flat plate is analyzed. Comparisons are made with experimental wind tunnel data of Dickinson.¹

collected in the low turbulence wind tunnel at DTNSRDC. All distances are normalized by the chord length. The Reynolds number was one-half million, based on chord length for both the experiments and computations. The computations did not include the effect of the wind tunnel walls, and can be thought of as modeling the flow of an appendage mounted perpendicularly between two channel walls of infinite extent. Only one-half of the channel was simulated, with a symmetry plane placed at mid-height of the channel. This mid-height agreed with that in the experiments. A Baldwin-Lomax type turbulence model was used to parameterize the shear stress, as explained in the next of this report.

The code used in the calculations called INS3D, for incompressible three-dimensional, was developed by Kwak et al.² to aid in the redesign of the space shuttle main engine. One of the most important aspects in solving the incompressible Navier-Stokes equations in primitive variables is to get a pressure field that guarantees a divergence-free velocity field. Various techniques have been proposed for doing this, including the Poisson equation and the fractional step method. A commonly used procedure is to choose the pressure field in such a way that the continuity equation is satisfied at the next time level. The new flow field will then be divergence free; however, this procedure, which typically involves a relaxation scheme iterating on pressure until the divergence-free condition is satisfied, can be very time consuming. To overcome this drawback, Chorin³ suggested using artificial compressibility in solving the continuity equation. This pseudocompressibility approach is incorporated in INS3D and is described further in a later section of this report. The resulting governing equations are solved using a beam-warming approximate factorization scheme, with second and fourth order dissipation terms to damp out the numerical instabilities. INS3D neglects the nonorthogonal viscous terms,² which will be zero provided the grid lines are orthogonal. Where the grid is nonorthogonal, it is assumed the nonorthogonal viscous terms are negligible. INS3D also assumes that the second and fourth order viscous damping terms do not affect the converged solution and that, once convergence has been achieved, the pseudocompressibility term in the continuity equation is small enough that a divergence-free flow field results. The accuracy of the results from INS3D, as composed with experimental data² lends credence to the validity of these assumptions.

NUMERICAL PROCEDURE

This section briefly describes the governing equations of INS3D and its assumptions, the method of solution, and the implementation of the boundary conditions. These subjects are described in another section of this report. This section also reviews the grid generation scheme used to discretize the flow field and the turbulence model used to parameterize the shear stress.

GOVERNING EQUATIONS

The Reynolds equations for unsteady, viscous incompressible flow with constant density may be written as

$$\frac{\partial u_i}{\partial x_i} = 0. \quad (1a)$$

$$\frac{\partial u_i}{\partial t} + \frac{\partial u_i u_j}{\partial x_j} = -\frac{\partial p}{\partial x_i} + \frac{\partial \tau_{ij}}{\partial x_j}. \quad (1b)$$

where t = time

x_i = Cartesian coordinate

u_i = corresponding velocity component

p = pressure

τ_{ij} = viscous shear stress tensor.

The viscous shear stress may be written as

$$\tau_{ij} = 2\mu S_{ij} - R_{ij}. \quad (1c)$$

where

$$S_{ij} = \frac{1}{2} \left(\frac{\partial u_i}{\partial x_j} + \frac{\partial u_j}{\partial x_i} \right), \quad (1d)$$

R_{ij} is the Reynolds stress, and μ is the coefficient of viscosity. According to the eddy-viscosity approach, R_{ij} is given by

$$R_{ij} = -\partial \mu_t S_{ij}. \quad (1e)$$

where μ_t is the turbulent eddy viscosity.

In the method of pseudocompressibility, the continuity equation is modified to the form

$$\frac{1}{\beta} \frac{\partial p}{\partial t} + \frac{\partial u_i}{\partial x_i} = 0. \quad (1f)$$

where $1/\beta$ is the pseudocompressibility. The inclusion of this term introduces pressure waves of finite speed into the fluid medium, whose wave speed would otherwise be infinity. These pressure waves die out as the solution reaches steady state.

The rate of propagation of the pressure waves is determined by the pseudocompressibility factor $1/\beta$. In addition, the rate at which the solution converges to steady state is also determined by $1/\beta$. Numerical studies² have shown that, for external flow problems, an acceptable range of β is between one and ten. In this study, a value of five was typically used. For internal flow problems, where the

pressure waves may reflect back and forth from the solid surfaces, the range of β is more restrictive. Guidelines for determining the lower and upper limits of β were presented. The lower limit is determined from the requirement that the rate at which the pressure waves propagate should be less than the rate of propagation of viscous effects. The upper limit of β is determined from the necessity to restrict the size of the approximate factorization term, which appears as a result of the beam-warming factorization scheme used to discretize the equations. Kwak et al.² give examples showing how the variation of β affects convergence.

Equations 1b and 1e form a hyperbolic set of equations, which can be solved using a standard time-marching technique. In the INS3D code, this technique consists of a beam-warming approximate factorization scheme with trapezoidal time differencing. As the solution reaches steady state, the time derivative of the pressure term vanishes, and the incompressible form of the Reynolds equations is recovered.

GRID GENERATION

For a simple geometry, such as the appendage-flat plate configuration considered in this study, the grid can be generated in two dimensions around the appendage in the (x-y) plane, and then stacked in the vertical (z) direction, using a suitable stretching routine. This procedure was used to generate the mesh system for the present study. The two-dimensional grid around the appendage was obtained with a code for generating the grid around airfoils using the Poisson equation (GRAPE). GRAPE, which was developed by Sorenson⁴ at NASA Ames, allows for control of mesh spacing at the boundaries and of the angle with which the grid lines intersect the boundaries.

Figure 1 shows the mesh system around the appendage used in the computations. There are 113 grid lines wrapped around the body with 56 grid lines extending away from the body. The first grid point is located 0.0005 chord lengths from the appendage surface. The appendage extends from $x = 0.0$ to $x = 1.0$. The grid extends a distance of 10 chord lengths away from the body in all directions. There are 29 grid points in the vertical direction (z), with the first grid point 0.0005 chord lengths away from the flat plate. The 28th grid point corresponds to a z value of 1.0 which is equivalent to the symmetry plane of the wind tunnel used in the experiments. Thus, the flow configuration is that of a two-dimensional channel in which an appendage is mounted so that both ends of the appendage are in contact with the two walls of the channel. Figure 2 shows the orientation of the coordinate system, with x in the streamwise direction, y along the flat plate, and z along the appendage.

BOUNDARY CONDITIONS

Explicit boundary conditions are used in the numerical algorithm. At the inflow boundary ($x = -10.0$), a two-dimensional channel inflow velocity profile is prescribed by assuming a one-seventh power law distribution. A boundary-layer thickness of 0.2 was found to give reasonably good agreement with the experimental results three-quarters of a chord length upstream of the appendage leading edge (Fig. 3). Near the flat plate, i.e., for $z < 0.05$, the numerically

predicted velocity profile is steeper than that observed experimentally, which translates into a relatively greater vorticity in the approaching boundary layer. The sensitivity of the secondary flow system to the incoming vorticity distribution is not known. A uniform pressure distribution is not known. A uniform pressure distribution is prescribed at the inflow boundary. These same boundary conditions are imposed on the lateral boundaries ($y = \pm 10.0$), under the assumption that they are far enough away from the appendage so that the profile has returned to a two-dimensional profile. Symmetry boundary conditions are applied at $z = 1.0$, which corresponds to the mid-height of the wind tunnel.

No-slip boundary conditions are applied at the appendage and at the flat plate surface. The pressure on the appendage and on the flat plate surfaces is determined under the assumption that the normal pressure gradient is zero, i.e.,

$$\frac{\partial \hat{p}}{\partial \hat{n}} = 0. \quad (2)$$

where \hat{n} is a vector normal to a wall.

Conditions for the downstream boundary are the most difficult ones to provide, and they require careful specification to avoid numerical instabilities and nonconvergence. For the lateral boundaries, the downstream boundary is assumed to be far enough away from the appendage so that the velocity profile has returned to a two-dimensional form, i.e., $v = w = 0$. The values of streamwise velocity and pressure are updated in the manner prescribed by Chang et al.² In this approach, a second-order upwind extrapolation is first used to update u on the exit plane. Next, these updated velocities are mass-weighted to conserve the inlet mass flux. A new pressure corresponding to these mass-weighted velocities is then determined to ensure conservation of momentum flux at the outflow.

TURBULENCE MODEL

Turbulence modeling for wing-body junction regions is complicated and not well understood. To simplify the analysis an algebraic eddy-viscosity model, proposed by Baldwin and Lomax⁵ is used. In this approach, an eddy viscosity is calculated for an inner and an outer region. The eddy viscosity for the inner region is based on the Prandtl-Van Driest formulation

$$(\mu_t) = \rho \ell^2 |\omega|, \quad (3)$$

where

$$\ell = ky[1 - \exp(-y^+/A^+)], y^+ = \rho u_\tau y / \mu. \quad (4)$$

and u_τ is the wall shear stress. The magnitude of the vorticity $|\omega|$ is given by

$$|\omega| = \left[\left(\frac{\partial u}{\partial y} - \frac{\partial v}{\partial x} \right)^2 + \left(\frac{\partial v}{\partial z} - \frac{\partial \omega}{\partial y} \right)^2 + \left(\frac{\partial \omega}{\partial x} - \frac{\partial u}{\partial z} \right)^2 \right]^{1/2}. \quad (5)$$

The eddy viscosity for the outer region is given by

$$(\mu_t)_{outer} = \rho K C_{cp} F_{wake} F_{kleb}(y), \quad (6)$$

where F_{wake} is the smaller of $Y_{max} F_{max}$ or $C_{wk} Y_{max} U_d^2 / F_{max}$.

F_{max} is the maximum value of the expression

$$F(y) = y|\omega|[1.0 - \exp(-y^+ / A^+)], \quad (7)$$

and Y_{max} is y at that point. Also

$$F_{kleb}(y) = [1 + 5.5(C_{kleb}y/Y_{max})^6]^{-1}. \quad (8)$$

The quantity U_d is the difference between the maximum and minimum values of vorticity in a given profile. The constants are assigned the following values: $A^+ = 26$, $C_{cp} = 1.6$, $C_{kleb} = 0.3$, $C_{wk} = 0.25$, and $K = 0.0168$.

As discussed by Mehta et al.,⁶ the above formulation gives $(\mu_t) = 0.0$ in the wake region when the wake is symmetric, because the Van Driest damping function, Eq. 4, depends on the vorticity on the centerline of the wake, which has the value of zero. Mehta et al.⁶ account for the zero value of μ_t in the wake region for symmetric wakes by modifying the length scale equation to give

$$(\ell)_{inner} = 0.4y[1.0 - \exp \{ - (y^+ / A^+) - (X^+ / A^+) \}] \quad (9)$$

with

$$X^+ = \begin{pmatrix} 0.00 & \text{if } x < 1.0 \\ (x - 1.0) & \text{otherwise} \end{pmatrix}.$$

In the outer region, the definition of $F(y)$ is replaced by

$$F(y) = y|\omega|[1.0 - \exp \{ - (y^+ / A^+) - (X^+ / A^+) \}]. \quad (10)$$

The eddy viscosity was determined at every point using both Eqs. 3 and 6. The smaller of the two eddy viscosities was then used in Eq. 1e. A zonal approach, similar to that used by Hung and Buning,⁷ was used to handle the three-dimensional corner flow configuration. First, the eddy viscosity related to each wall was calculated as described above. For $z > abs(y)$, the eddy viscosity as determined from the appendage was selected; for $z < abs(y)$, the eddy viscosity as determined from the flat plate was used. For $z = abs(y)$, the eddy viscosity is determined from an average of the immediately adjacent points.

RESULTS AND DISCUSSION

This section presents the numerical calculations for the flow around an appendage mounted on a flat plate and compares these results with Dickinson's wind-tunnel experimental data for the modified appendage shape. This shape has a 1.5:1 elliptical nose and a NACA 0020 tail joined at maximum thickness. The resulting appendage has a chord of 10.2 inches and a thickness of 2.4 inches.

A right-hand coordinate system is used, such that x is in the streamwise direction, y is along the flat plate, and z is normal to the flat plate, i.e., along the appendage (Fig. 2). The appendage occupies the region from $x = 0.0$ to $x = 1.0$, with the inflow at $x = -10$. All distances are nondimensionalized by the chord length, and the velocities are nondimensionalized by the free-stream velocity.

Both the experiments and computations were performed at a Reynolds number, based on chord length, of approximately one-half million. A one-seventh power law, with a boundary layer thickness of 0.2, was used to provide the inflow conditions for the computations. As mentioned above, the inflow for the computations was 10 chord lengths upstream of the appendage. This profile was found to yield a reasonably good comparison with the experimentally measured inflow profile at $x = -0.75$, as shown in Fig. 3. The computations do not include the effects of the wind tunnel walls, which are located at a distance of 1.2 chord lengths away from the appendage. The results shown in the following sections of this report were produced using the graphical display routine PLOT3D, developed at NASA Ames.⁸

All the experimental data and much of the interpretation of the physics of the flow field are from Dickinson,¹ who also contributed to the interpretation of the numerical results.

PRESSURE DISTRIBUTION

Figure 4 compares the C_p distributions on the flat plate for two y values corresponding to the symmetry plane, $y = 0.0$, and $y = 0.147$. The experimental and numerical values are seen to compare quite well. The values of C_p for $y = 0$ exhibit the steep adverse pressure gradient responsible for the skewing of the vorticity in the incoming boundary layer. The slight rise at $x = -0.2$ corresponds to the leading edge separation point, as can be seen in Figs. 5 and 8.

For $y = 0.147$, the flow accelerates around the appendage, with a resulting drop of pressure, reaching a pressure minimum near the maximum appendage thickness. This area is followed by a region of pressure recovery as the appendage geometry thins. The high pressure region near the trailing edge is due to the stagnation point located there.

OIL FLOW VISUALIZATION

Figure 6 shows the oil-film flow visualization for the wing-flat plate region. The numerical flow simulation results are presented for comparison in Figs. 7 and 8. Ahead of the appendage, the oil streaks follow a fairly straight line. As they approached the appendage, the oil streaks diverge and wrap around the

appendage in the characteristic horseshoe vortex pattern. Figure 8 shows the details of the leading edge separation; the location of the separation point is about 0.2 chord length upstream of the leading edge, which is about twice the distance found in the experiments.

Both the experimental and numerical results show primary separation lines springing from the separation point and trailing off downstream. In addition, the experiments show a second line between the separation line and the leading edge. This second line is interpreted by Dickinson,¹ not as a separation line, but as a shear-stress gradient line, dividing a region of high shear near the foil from an area of lower shear outside. The shear-stress gradient line wraps around the leading edge and merges with the primary separation line along the foil. This interpretation is consistent with the numerical results, which show only one separation system.

Figure 6 shows a V-shaped pattern near the trailing edge, which Dickinson¹ ascribes to a small counter-rotating vortex carrying oil into the corner, where it runs downstream and leaves the appendage. A scoured region, caused by the downwash of the wake of the appendage, appears inside this V-region, as seen in Fig. 6. The numerical results also show this V-region in Fig. 7.

As already mentioned, the numerical flow simulation captures most of the essential features of the horseshoe vortex system, including the presence of only one separation system at the leading edge and the V-shaped region at the stern. However, the lateral extent of the numerical horseshoe system, as determined by the location of the primary separation lines, is overpredicted by almost a factor of two compared to the experiments. At first, this difference was thought to be the result of the wind tunnel wall blockage, which is not accounted for in Dickinson's experiments. Experiments done by Devenport and Simpson,⁹ who used inserts to eliminate blockage-induced pressure gradients around the appendage, found essentially the same shape for the horseshoe vortex. These experiments were conducted on the same appendage as that used by Dickinson, with approximately the same Reynolds number. Although the cause of the discrepancy cannot be stated conclusively, one likely explanation is that the simple Baldwin-Lomax turbulence model, designed originally for two-dimensional flows, cannot handle such complicated geometries as corner flow. As discussed in greater detail later in this report, experiments by Shabaka and Bradshaw¹⁰ have shown that, in a large area of an appendage-flat plate corner region, the turbulent shear stresses are of opposite sign to the mean velocity gradient, making the eddy-viscosity calculation method unsuitable. Bradshaw et al.¹¹ conclude that, except for rough calculations, nothing short of a full Reynolds stress turbulence model will accurately predict the decay of this skew-induced secondary flow.

Another possible cause of discrepancy between the computed and measured sizes of the horseshoe vortex involves the smoothing terms. In other studies¹² of flow around wings, these terms have been shown to affect the boundary-layer development, and thus the shear stress, and consequently the size of the separation region. The surface shear stress may also be in error due to the grid spacing on the solid surface, which was given in an earlier section of this report as 0.0005. This value is almost an order of magnitude greater than that typically used.⁶ As mentioned earlier, about 185,000 grid points were used in the calculation, which

approaches the maximum allowable on the Cray X/MP 4-8 computer on which the calculations were performed. A finer grid resolution near the wall would have required sacrificing grid resolution in the flow field, with a possible reduction in accuracy of the flow-field variables. Given the results of this study, additional runs with finer near-wall grid resolution would seem appropriate.

VELOCITY

This section compares experimental and computed velocities at the three planes, $x = 0.18, 0.75$, and 1.50 , corresponding to maximum thickness location, three-quarters chord length, and one-half chord length downstream of the trailing edge. The flow regimes of these three streamwise locations are substantially different and thus provide a good basis for comparison of the experimental and numerical results. The experimental and numerical mean velocity contours at each x station are plotted to the same scale; the cross-flow velocity vectors are also plotted to the same scale.

Cylindrical hot-film probes were used to collect the data. Dickinson¹ states that as a worst case, in areas of high shear, the mean velocities are accurate within $\pm 2.5\%$ of the free-stream velocity with a 95% confidence level. In regions of low shear, the accuracy is estimated to be $\pm 1.5\%$. This error estimate includes the effect of positioning.

Plane $x = 0.18$

Figures 9 and 10 show the experimental and numerical streamwise velocity contours, which agree fairly well. Both figures exhibit a two-dimensional region of the foil ($z > 0.3$) and of the flat plat ($y > 0.4$), with a uniform transition in the juncture region. Evidence of the horseshoe root vortex is seen in a small "kink" in the contours close to the wall. This kink is also visible in Figs. 11 and 12, which present velocity profiles of u vs. z for $y = 0.1471$ and $y = 0.1716$, respectively.

The experimental and numerical cross-flow velocity vectors, Figs. 13 and 14, both show an outflow in the two-dimensional wall and appendage region. In the corner region the flow is down (in the negative z direction) along the appendage and outward (in the positive y direction) along the wall; this pattern is the result of the secondary-flow vortex. High v velocities are seen close to the wall for both experiments and computations.

Plane $x = 0.75$

Figures 15 and 16 show the streamwise velocity contours at $x = 0.75$, which are seen to be considerably different from those at $x = 0.18$. Both experimental and computational results show a thin boundary layer developing on the appendage. The flow of high velocity fluid into the corner, visible in both figures, is the results of the horseshoe root vortex. The overturning of the numerical velocity contours near the wall can likewise be attributed to the secondary flow vortex. Much of this overturning occurs for z less than 0.01 , which is the lowest plane at which measurements were taken. The fact that measurements were not conducted below the plane $z = 0.01$ may explain why overturning is not observed

in the experimental data. The numerical results also show evidence of a small counter-rotating vortex in the corner region.

Velocity profiles of u vs. z for $y = 0.0588, 0.098$, and 0.245 are shown in Figs. 17, 18, and 19. The y location of the appendage surface for $x = 0.75$ is about 0.05 . For $y = 0.0588$, Fig. 17, the experimental results show a small region of flow reversal near the wall, caused by the secondary root vortex, as explained above. This phenomenon was also observed by Devenport and Simpson⁹ in their wind tunnel study of appendage-flat plate flow. The numerical results show qualitatively the same trend, but on a much larger scale. The discrepancy between observed and predicted mean velocities for $y = 0.0588$ may be due to the fact that the simple Baldwin-Lomax turbulence model cannot handle this highly complicated, three-dimensional region in the immediate vicinity of the corner. As y increases, the correspondence becomes increasingly better, as seen in Figs. 18 and 19. The slight flow reversal near the wall shows the effect of the horseshoe vortex, which at this location extends to about $y = 0.45$.

The experimental and numerical cross-flow velocity vectors, Figs. 20 and 21, both show flow generally toward the foil. This flow is induced by the geometry of the foil, which thins behind the location of maximum thickness. The numerical results show a region of flow in the positive y direction very near the flat plate, corresponding to the secondary root vortex. This positive y direction flow is not seen in the experiments. As discussed previously, the size of the computed horseshoe vortex is larger than that observed experimentally, and thus one would expect to see more evidence of the root vortex system. Also, most of the positive flow occurs below $z = 0.01$, which is the lowest plane at which experimental measurements were made. Thus, one possible explanation for not observing the positive y -direction flow in the experiments is that the measurements did not extend close enough to the flat plate.

Plane $x = 1.5$

This plane is situated in the wake of the appendage. The mean velocity contours, Figs. 22 and 23, display the same general features as those discussed for $x = 0.75$, but the downward movement of high velocity fluid is considerably less severe. The experimental results show a distortion in the contours around $y = 0.2$ caused by the outflow of low-velocity fluid. This feature is not as noticeable in the numerical contours. Velocity profiles of u vs. z for three y locations, $y = 0.0245, 0.049$, and 0.2206 , are shown in Figs. 24 through 26. For $y = 0.0245$, which is very near the wake centerline, the observed and computed u values away from the flat plate, i.e., for $z > 0.35$, are reasonably well predicted. Closer to the flat plate, correspondence becomes increasingly worse, indicating the inability of the simple turbulence model to predict the complex flow regime of a downwash caused by the secondary flow pumping fluid toward the walls. As y increases, and this phenomenon becomes less severe, the observed and computed velocities are in better agreement, as shown in Figs. 25 and 26 which give the velocity profiles for $y = 0.049$ and 0.226 , respectively.

The cross-flow velocity vectors, Figs. 27 and 28, show a junction induced secondary flow consisting of a downward movement of fluid near $y = 0$, and an outward flow along the wall. In the central region of the flow field, away from the

wake and the wall, the magnitude of the measured cross flow is within the error bounds of the data (roughly the size of the arrowhead). The experimental results show a vortex-like circulation centered at about $z = 0.1, y = 0.2$; the numerical results also show this circulation, with a center at $z = 0.06, y = 0.25$. Since no velocity is associated with this feature, it is doubtful that much importance should be placed on the comparison of the experimental and computed feature associated with it.

SUMMARY AND CONCLUSIONS

This report has described the application of a three-dimensional steady Reynolds equation solver to the problem of an appendage mounted on a flat plate. The code, INS3D, was originally developed by Kwak et al.² to aid in the redesign of the space shuttle main engine. INS3D handles the pressures using a pseudo-compressibility approach to obtain a steady-state solution. The governing equations are solved using a beam-warming approximate factorization scheme, with second and fourth order smoothing terms to damp out the numerical instabilities.

The grid discretization for the appendage-flat plate problem was performed using GRAPE⁴ to generate the grid in one x-y plane, and then to stack these grids in the z direction. A total of 185,000 grid points was used in the calculations, which were performed on the Cray X/MP 4-8 computer at NASA Ames Research Center. The results of numerical computations were compared with those from wind tunnel experiments conducted by Dickinson¹ in the DTNSRDC low-turbulence wind tunnel. The Reynolds number, based on chord length, for both the experiments and computations was one-half million. The inflow velocity profiles (Fig. 3) are in reasonable agreement. The computations did not include the effects of wind tunnel walls and can be thought of as modeling the flow of an appendage mounted perpendicularly between two channel walls of infinite extent. Only one-half the channel was simulated, with a symmetry plane placed at mid-height of the channel. This mid-height agreed with that of the experiments. A Baldwin-Lomax model, modified to account for the presence of two walls, was used to parameterize the shear stresses.

Comparisons between experimental and computed results are given for pressure and oil-film flow visualization; in addition, mean and cross-flow velocities are compared at three x stations, $x = 0.18, 0.75$, and 1.5 . The C_p distribution on the flat plate (Fig. 4) reveals reasonably good agreement between experimental and computed values. The numerically simulated flow visualizations (Figs. 7 and 8) show qualitatively the same features as the experiments (Fig. 6), but the predicted lateral extent of the horseshoe vortex is too large by a factor of 1.5 or 2.

Mean and cross-flow velocities are presented in Figs. 9 through 28. For $x = 0.18$, mean velocities agree quite well. For $x = 0.75$ and $x = 1.5$ the predicted mean velocity contours show the essential features of the flow, including the movement at high velocity of fluid into the corner, the ejection of low velocity fluid away from the appendage, and the development of the relatively thin boundary layer on the appendage, as compared to that on the flat plate. In the immediate vicinity of the corner, i.e., for $y < 0.1$ (maximum chord thickness is 0.24), the predicted profiles of u vs. z do not agree well with the experimental data; for y greater than 0.1, the agreement improves. Note that the y coordinate of the u

vs. z profiles presented here is within the lateral extent of the horseshoe vortex (about $y = 0.45$), thus giving evidence that the present model has some predictive capabilities other than in the strictly two-dimensional region of the flow.

The predicted cross-flow velocities show qualitatively the same features as the experimental values and are generally correct in magnitude within a factor of two. Typically, these cross-flow velocities are on the order of one-tenth the size of the mean velocities, making them harder to predict. The numerical cross-flow velocities show more evidence of the secondary root-vortex system, including a recirculation region near the flat plate that is generally not observed in the experiments. The size of the horseshoe vortex is overpredicted compared to the experiments.

In summary, the results presented here show that a simple algebraic eddy-viscosity model, such as the Baldwin-Lomax approach, can capture many, if not all, of the essential features of wing-flat plate corner flow. However, this model cannot handle the flow in the immediate corner region and tends to overpredict the size of the horseshoe vortex. Since the Baldwin-Lomax approach has difficulty in capturing the separated regions of 2-D supersonic compression ramp flows,¹³ its poor performance for the 3-D appendage-flat plate system is not too surprising. As mentioned previously, Shabaka and Bradshaw¹⁰ discuss measurements showing that, over a large part of the wing-flat plate corner region, the turbulent shear stresses are of opposite sign to the mean velocity gradients, thus, throwing in serious doubt the ability of the eddy-viscosity approach to predict the Reynolds stresses accurately. Since the gradients of Reynolds stress are generally in such a direction as to weaken the streamwise vortex,¹¹ it follows that calculations based on the eddy-viscosity approach would be unable to predict the decay of the secondary flow and would tend to overpredict the size of the horseshoe vortex. This conclusion agrees with the results of this study which found that the secondary flow system alongside the appendage was considerably stronger than that indicated by the experiments. Bradshaw et al.¹¹ state that, except for rough calculations, nothing short of a full Reynolds stress closure model will accurately predict the decay of a skew-induced secondary flow. It is, however, felt that the comparisons presented here show that the eddy-viscosity approach can provide useful information on many aspects of the wing-flat plate problem such as the pressure distribution and can provide qualitative indications of the mean and cross-flow velocities.

ACKNOWLEDGMENTS

The author wishes to thank Dr. Dochan Kwak for his advice and assistance in the use of the INS3D flow solver during the author's six-month visit at NASA Ames Research Center. Dr. Samuel Shanks and Mr. Stuart Rogers also provided valuable assistance in running INS3D and gave many helpful suggestions which greatly facilitated the application of the code to the wing-appendage problem. In addition to providing the experimental data, Dr. Stuart Dickinson helped interpret the numerical results and showed how they agreed or disagreed with the experimental data. Mr. Paul Granville provided helpful comments.

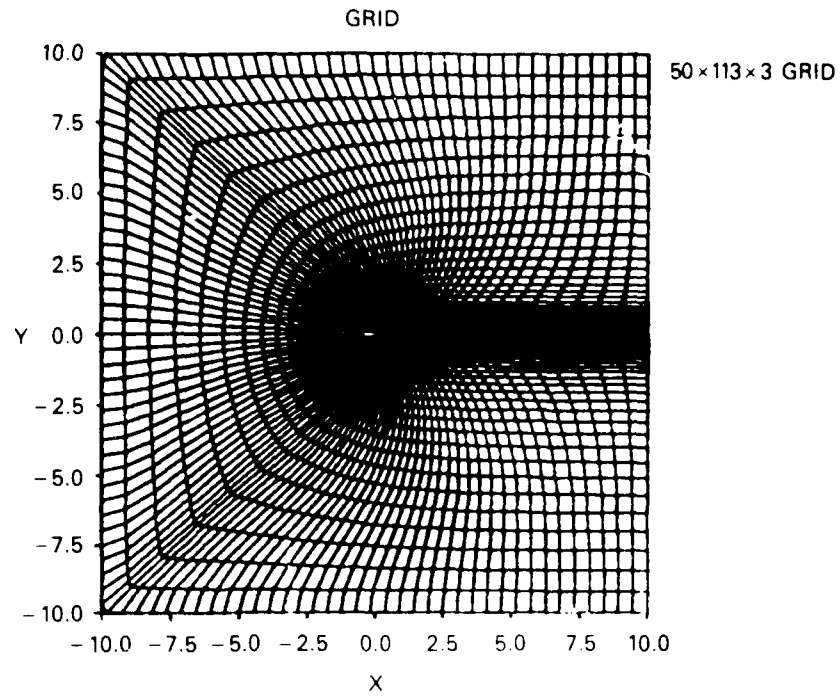


Fig. 1. C grid used in numerical computations.

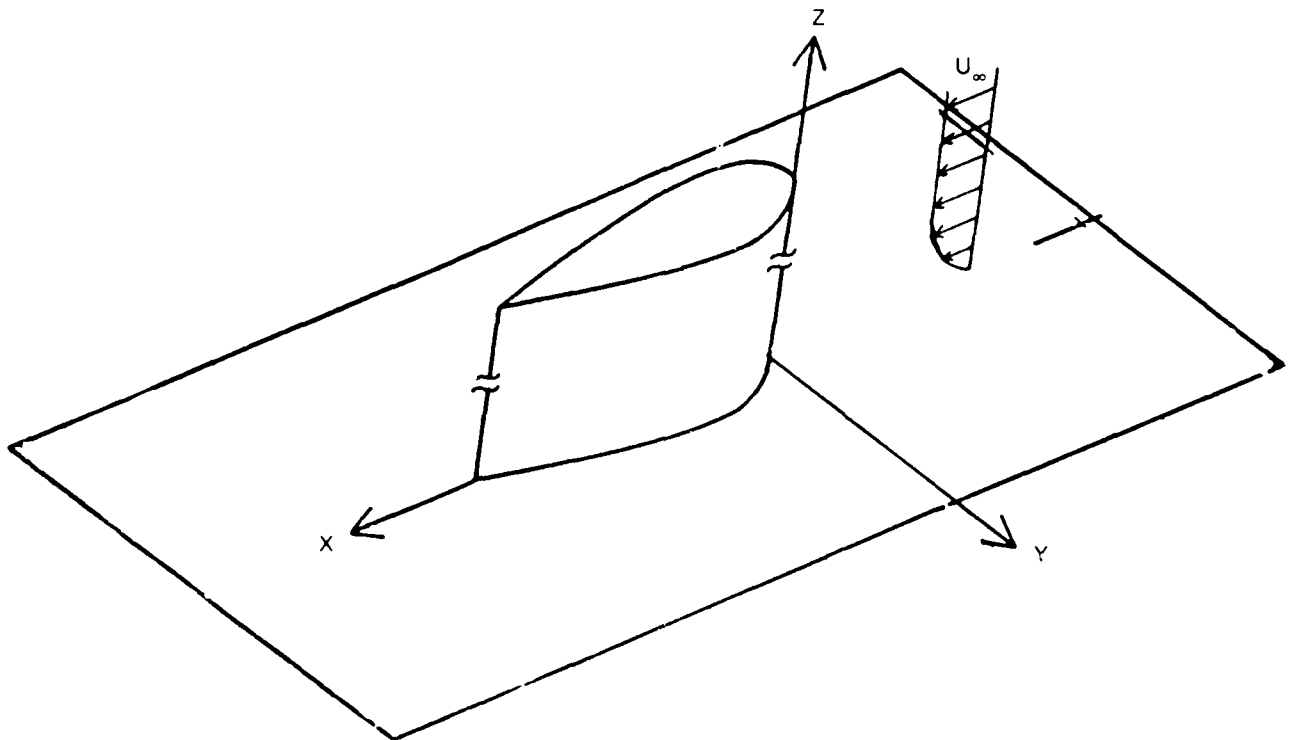


Fig. 2. Orientation of grid system.

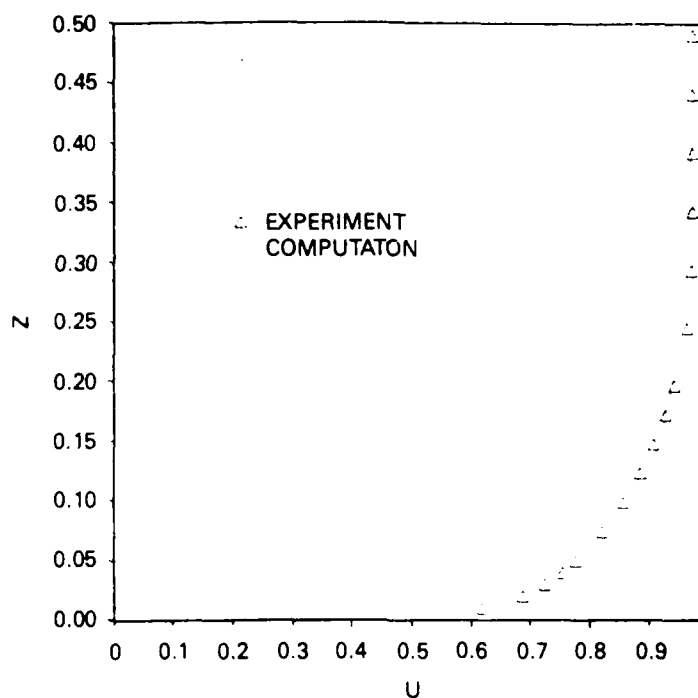


Fig. 3. Experimental and numerical mean velocity profiles (u vs z) for $x = -0.75$ and $y = 0.0$.

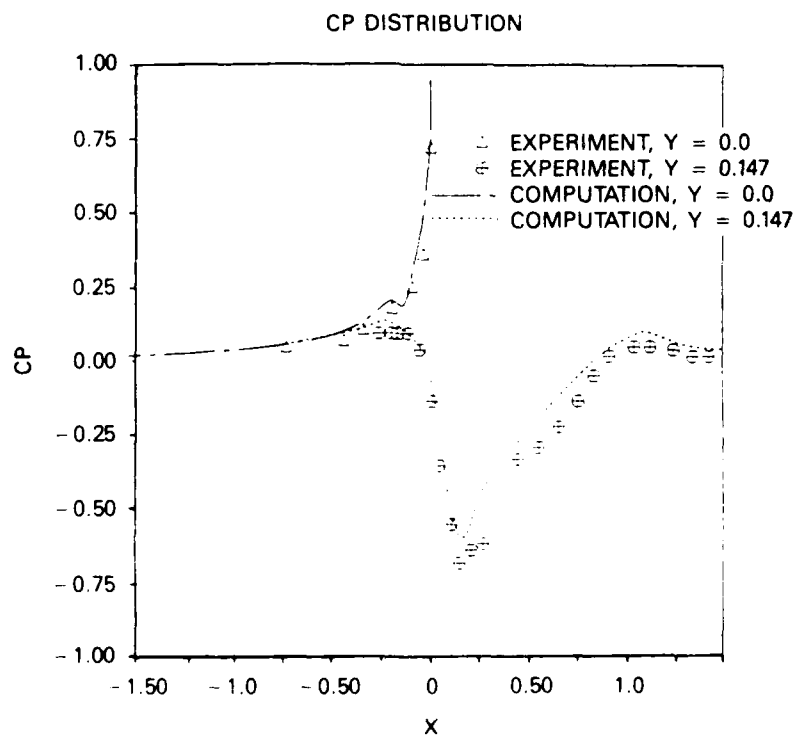


Fig. 4. Pressure distribution on flat plate near appendage.

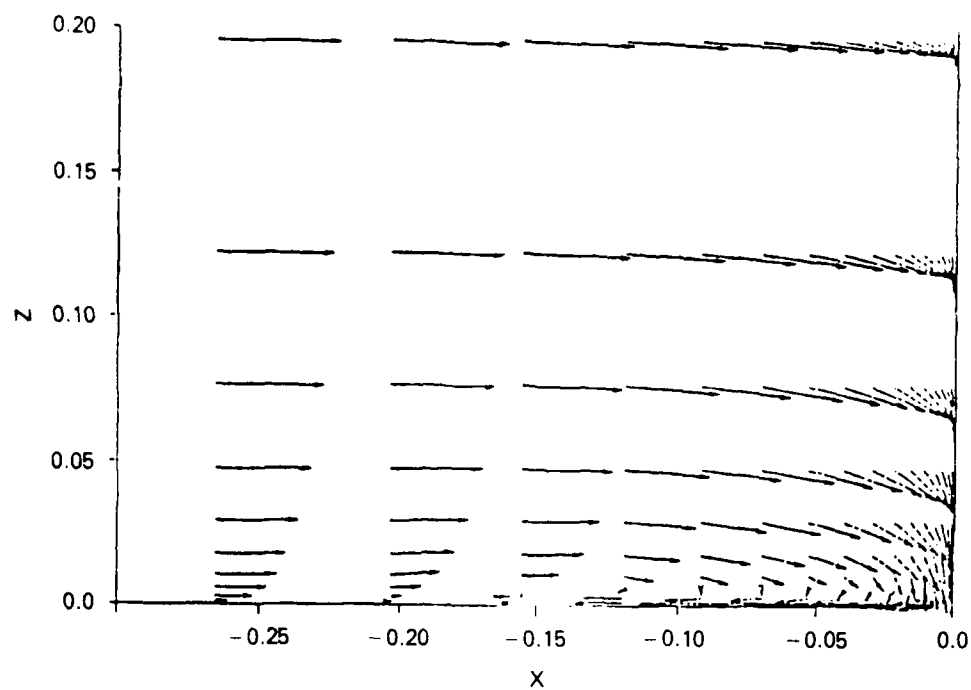


Fig. 5. Velocity vectors in the symmetry plane $y = 0$, ahead of wing.

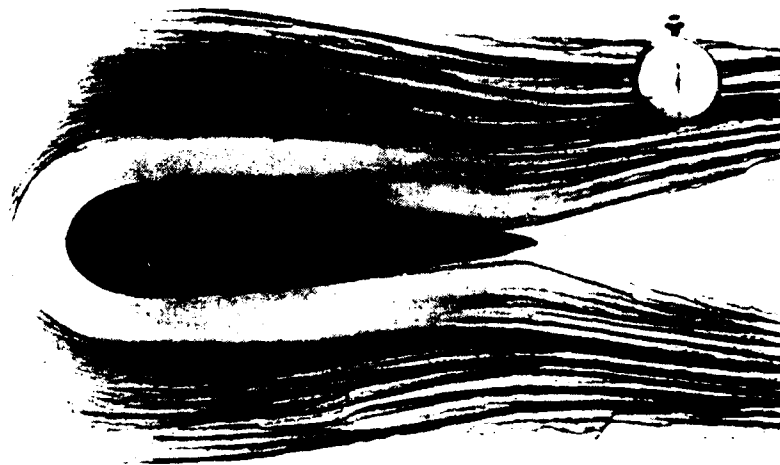


Fig. 6. Oil film flow visualization on flat plate (Dickinson 1986).

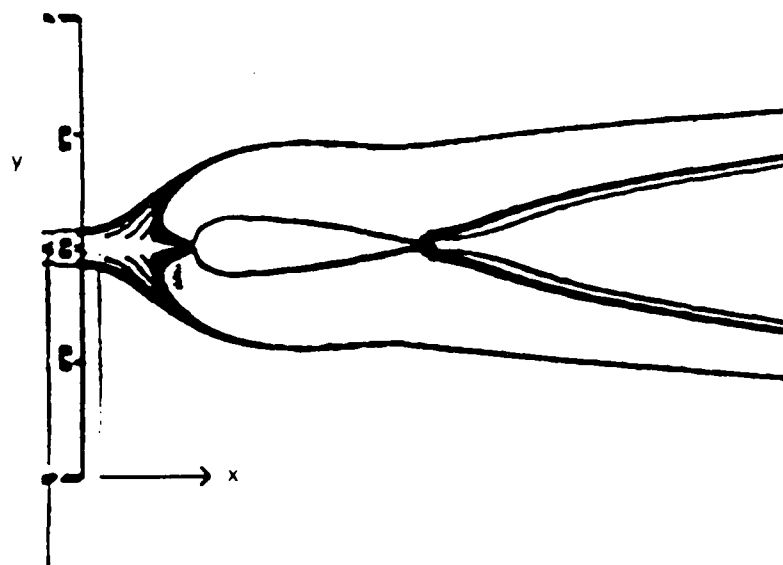


Fig. 7. Numerical flow simulation on flat plate, $z = 0$.

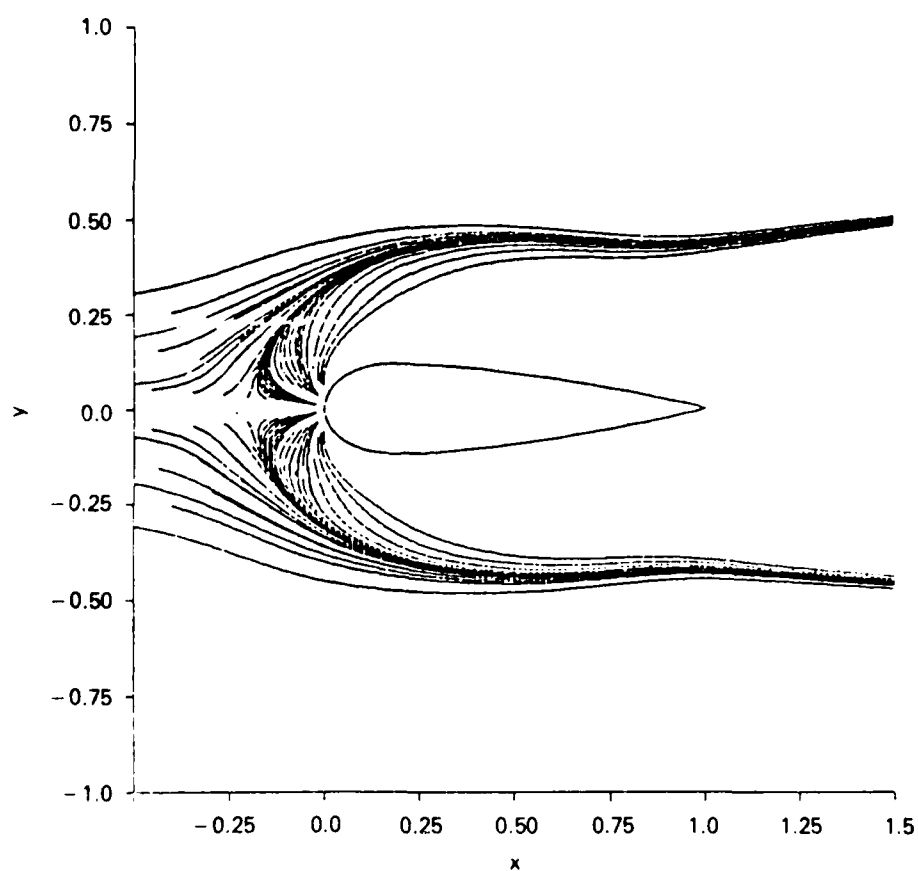


Fig. 8. Numerical flow simulation, showing detailed streamlines at leading edge on flat plate $z = 0$.

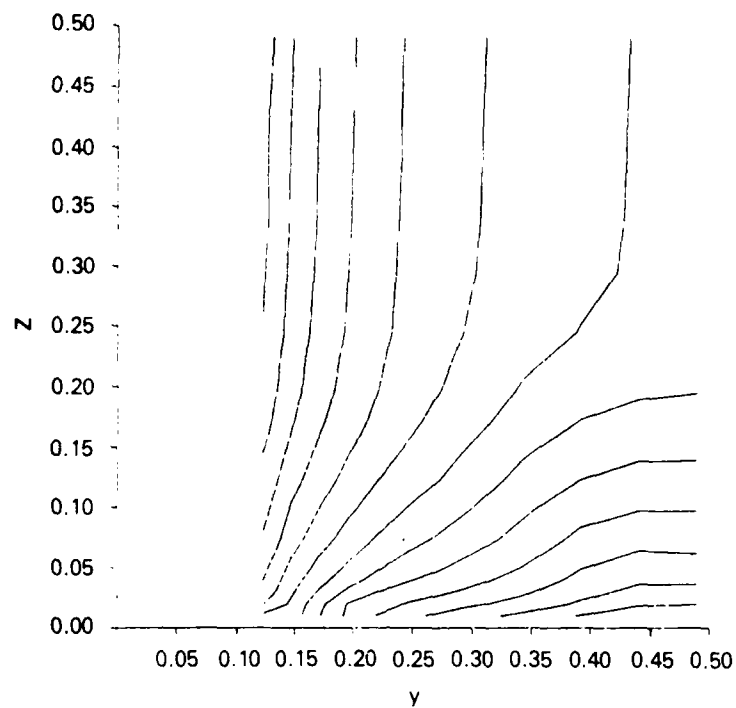


Fig. 9. Experimental mean velocity contours at $x = 0.18$ (Dickinson 1986).

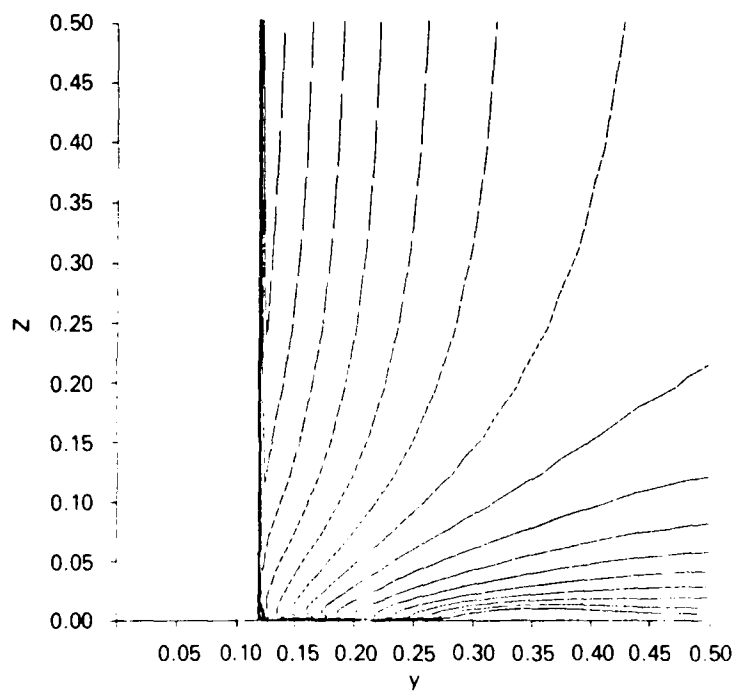


Fig. 10. Numerical mean velocity contours at $x = 0.18$.

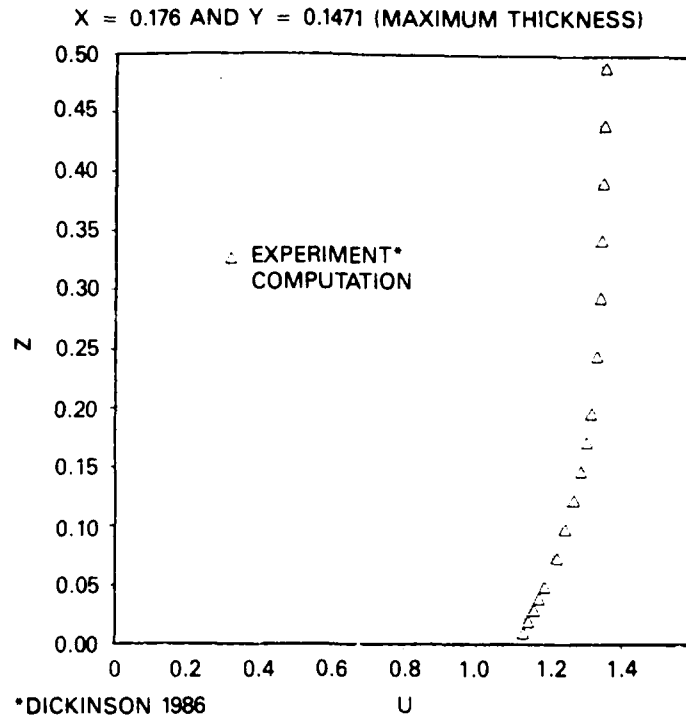


Fig. 11. Experimental and numerical mean velocity profiles (u vs z) at $x = 0.176$ and $y = 0.1471$.

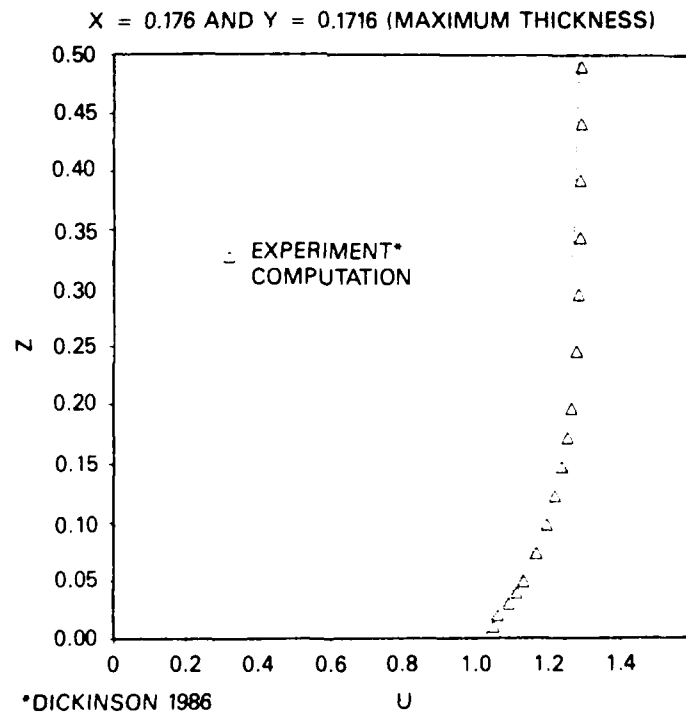


Fig. 12. Experimental and numerical mean velocity profiles (u vs z) at $x = 0.176$ and $y = 0.1716$.

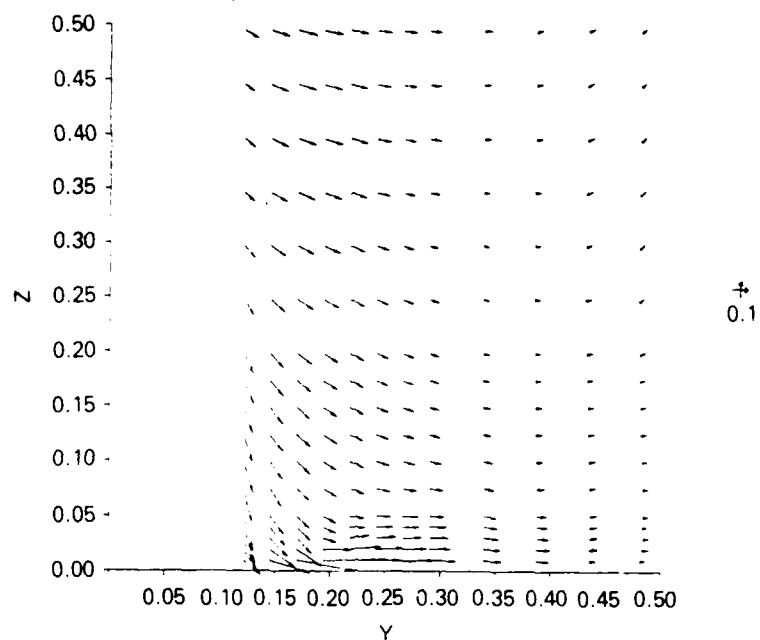


Fig. 13. Experimental cross-flow vectors at $x = 0.18$ (Dickinson 1986).

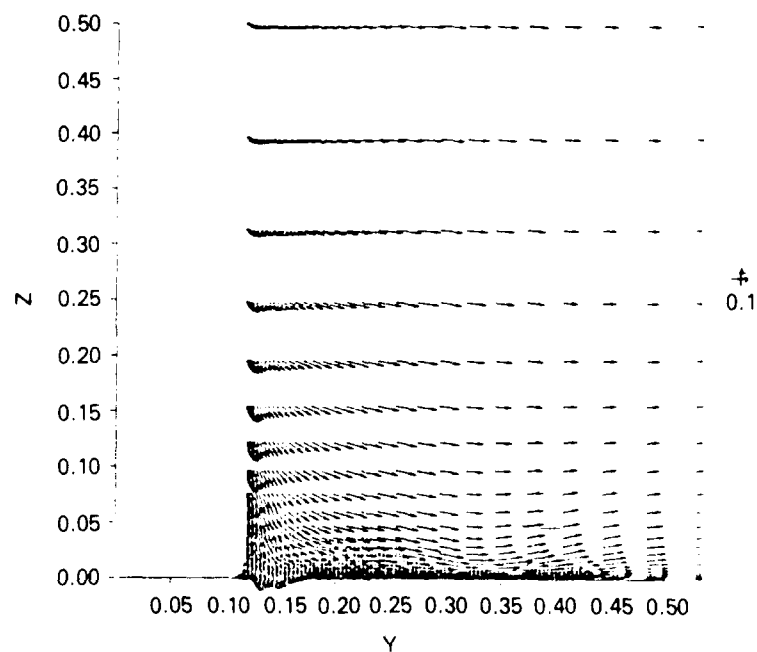


Fig. 14. Numerical cross-flow velocity vectors at $x = 0.18$.

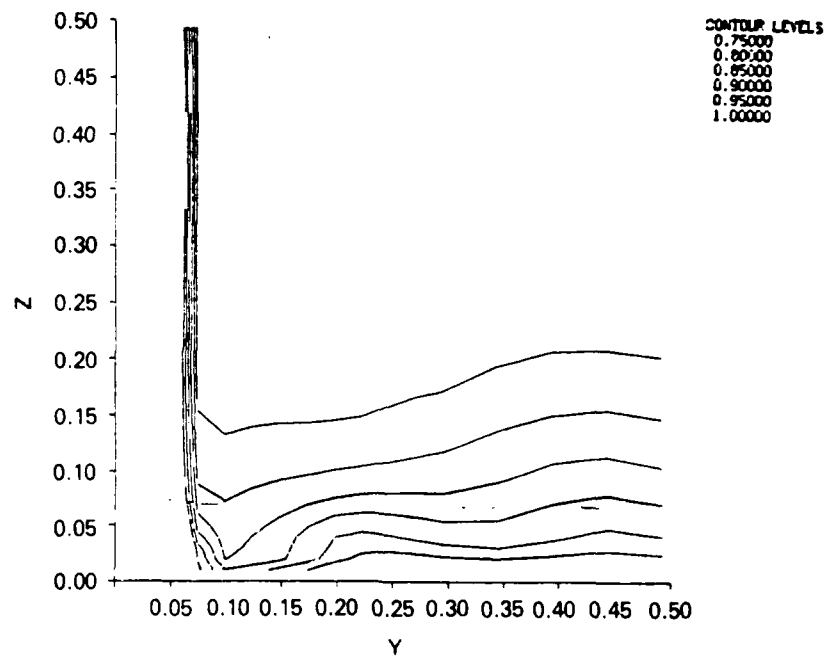


Fig. 15. Experimental mean velocity contours at $x = 0.75$ (Dickinson 1986).

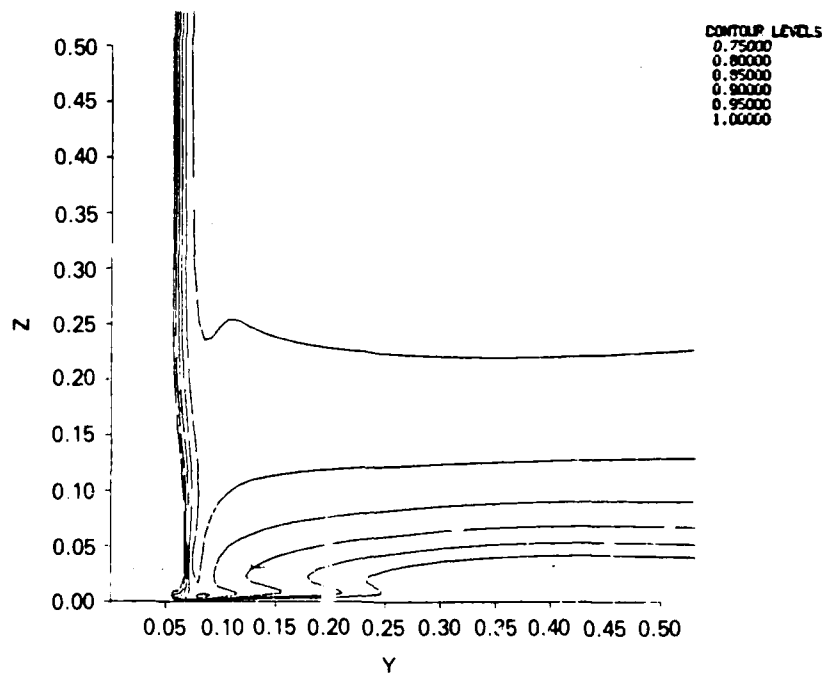


Fig. 16. Numerical mean velocity contours at $x = 0.75$.

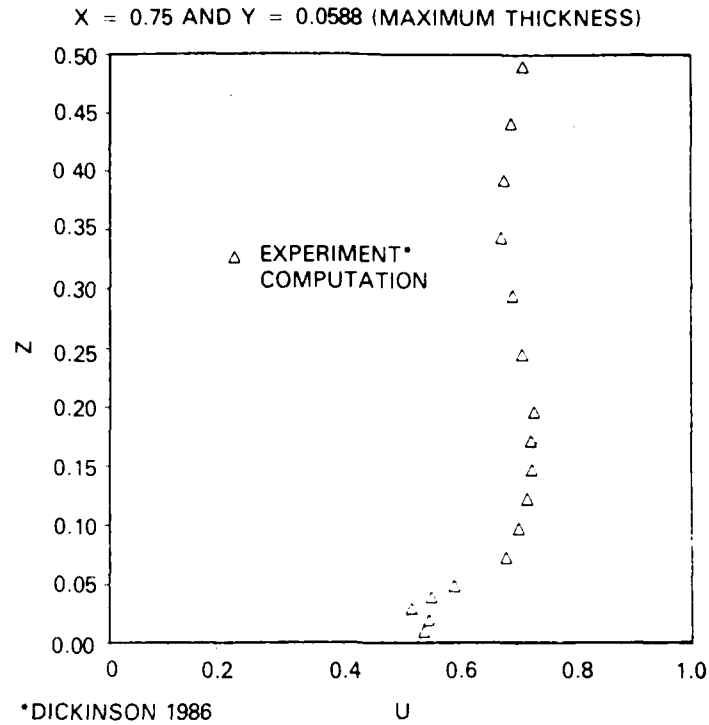


Fig. 17. Experimental and numerical mean velocity profiles (u vs z) for $x = 0.75$ and $y = 0.0588$.

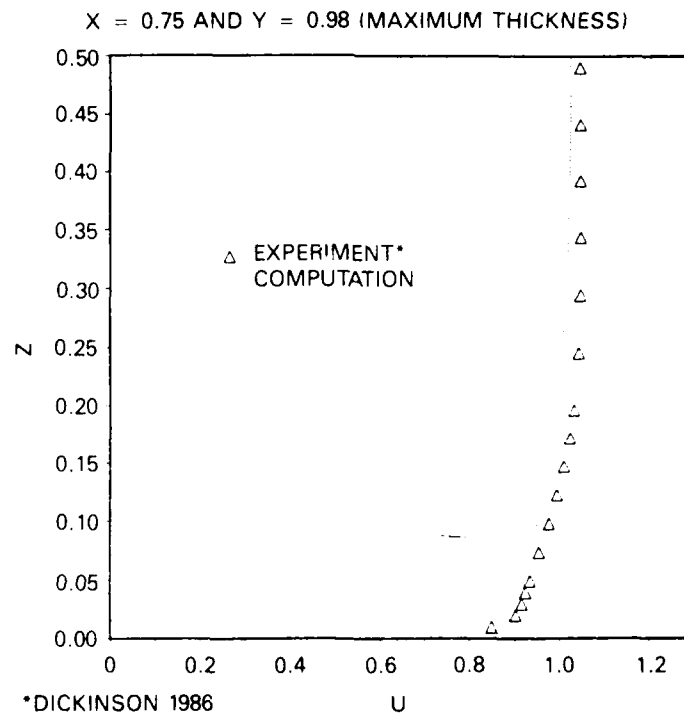


Fig. 18. Experimental and numerical mean velocity profiles (u vs z) for $x = 0.75$ and $y = 0.098$.

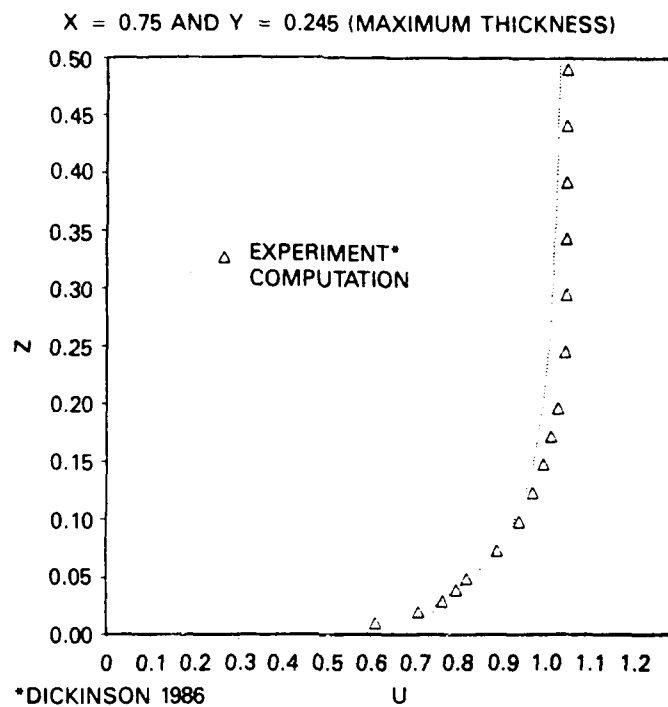


Fig. 19. Experimental and numerical mean velocity profiles (u vs z) for $x = 0.75$ and $y = 0.245$.

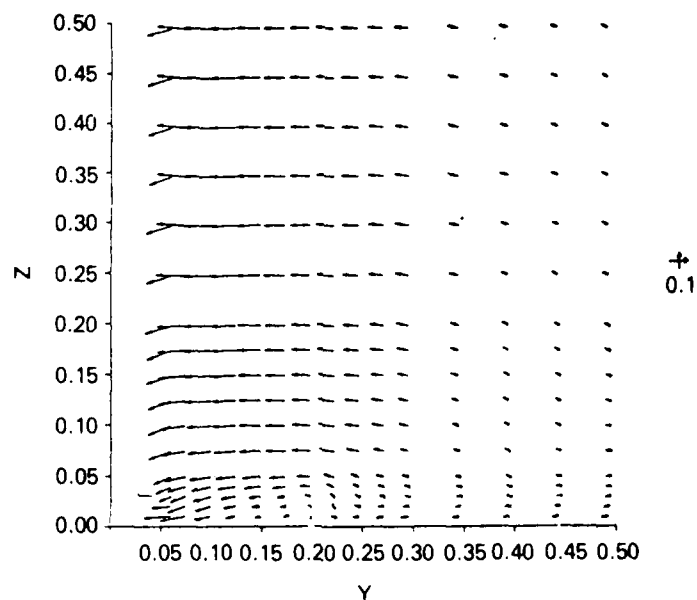


Fig. 20. Experimental cross-flow velocity vectors at $x = 0.75$ (Dickinson 1986).

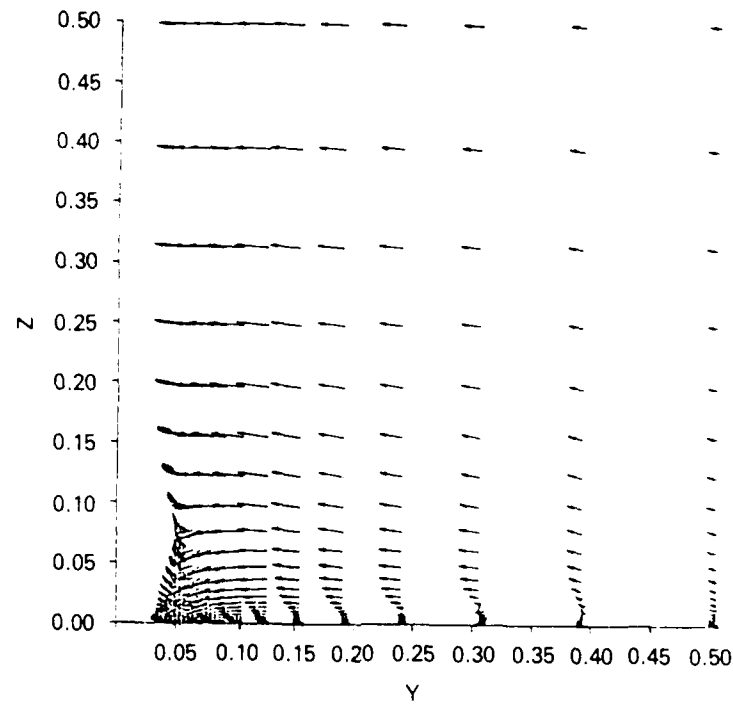


Fig. 21. Numerical cross-flow velocity vectors at $x = 0.75$.

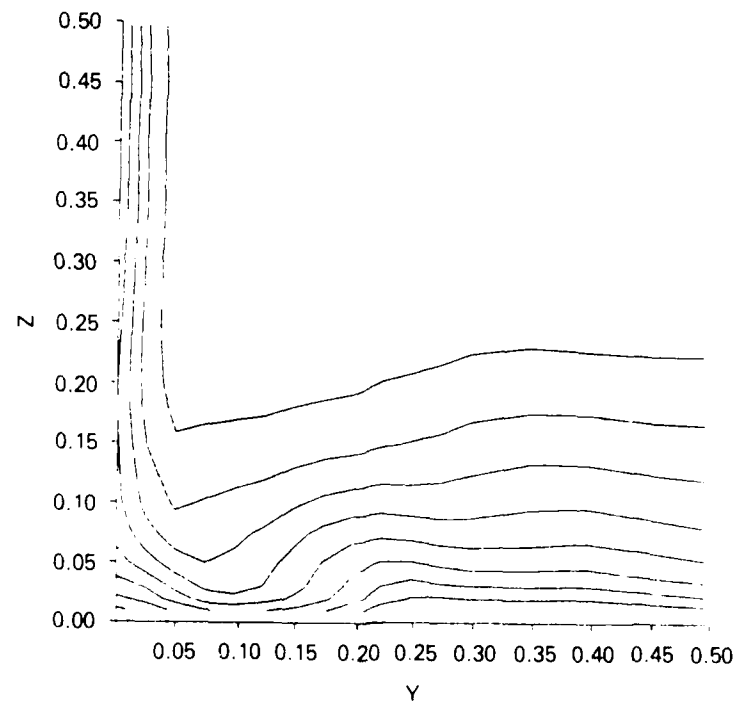


Fig. 22. Experimental mean velocity contours at $x = 1.5$ (Dickinson 1986).

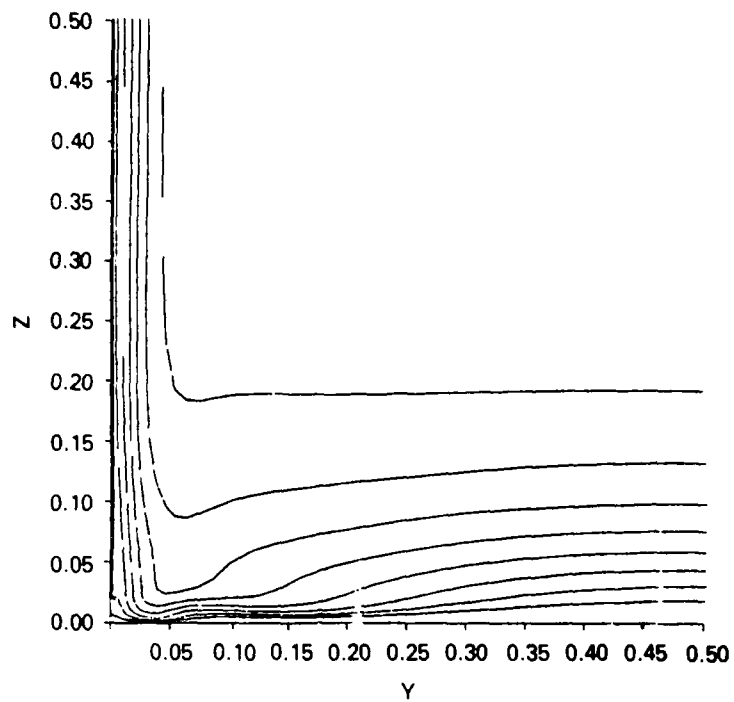


Fig. 23. Numerical mean velocity contours at $x = 1.5$.

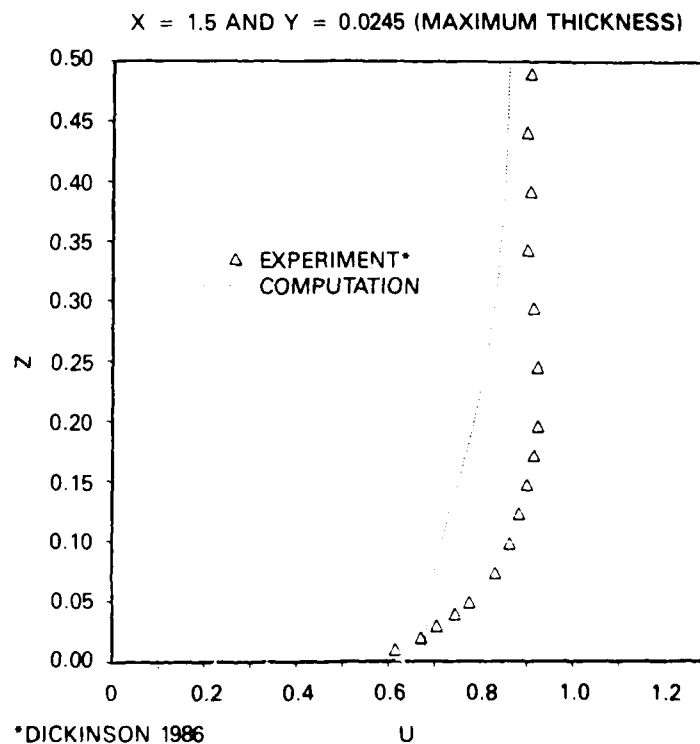


Fig. 24. Experimental and numerical mean velocity profiles (u vs z) for $x = 1.5$ and $y = 0.0245$.

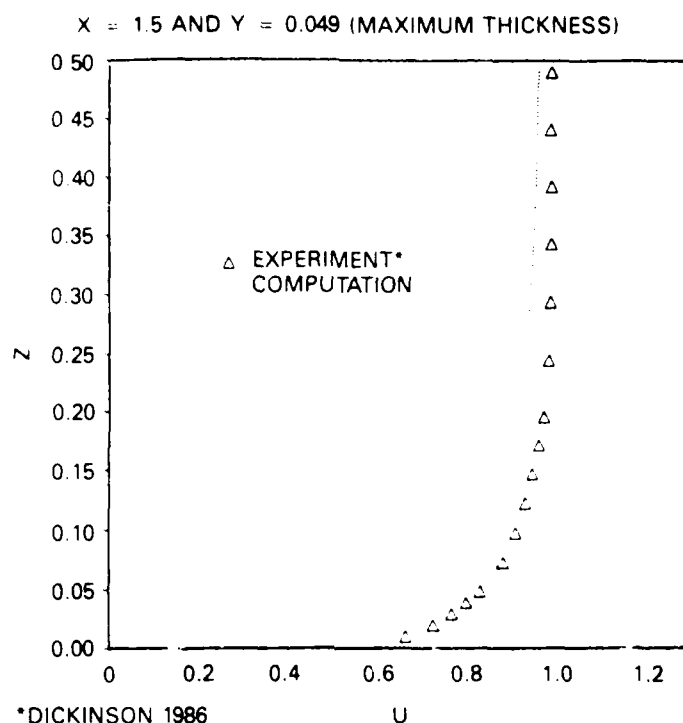


Fig. 25. Experimental and numerical mean velocity profiles (u vs z) for $x = 1.5$ and $y = 0.049$.

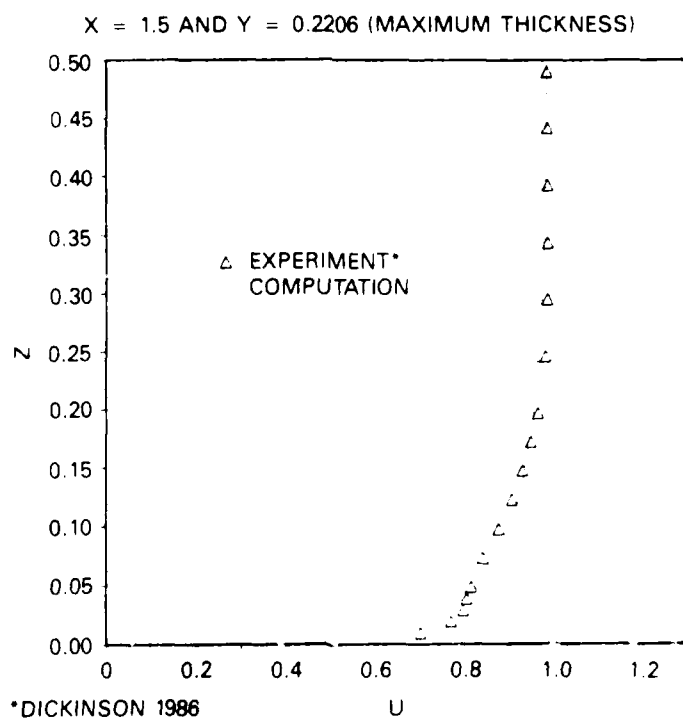


Fig. 26. Experimental and numerical mean velocity profiles (u vs z) for $x = 1.5$ and $y = 0.2206$.

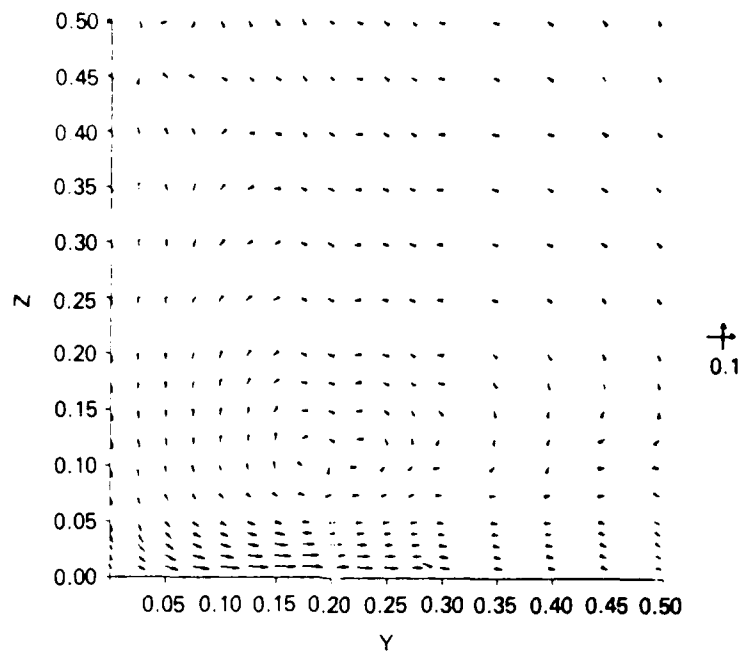


Fig. 27. Experimental cross-flow velocity vectors at $x = 1.5$ (Dickinson 1986).

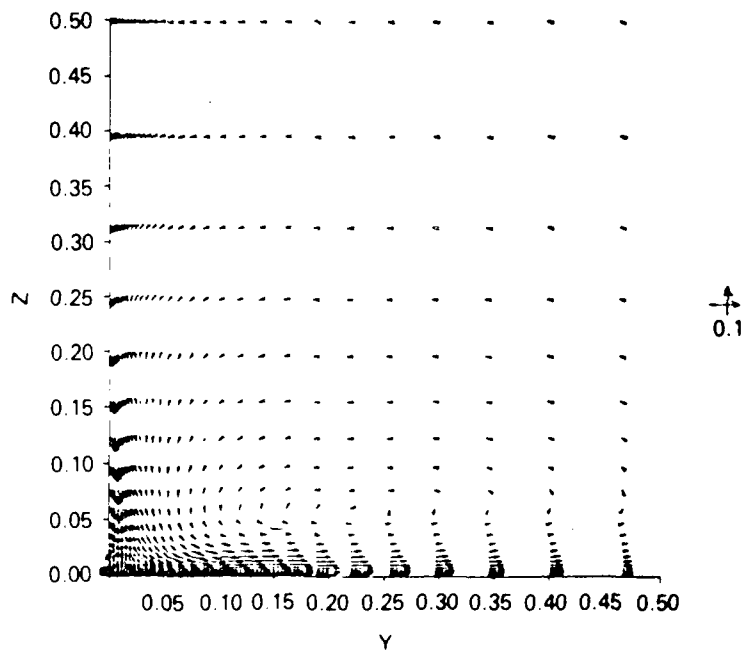


Fig. 28. Numerical cross-flow velocity vectors at $x = 1.5$.

REFERENCES

1. Dickinson, S.C., "An Experimental Investigation of Appendage-Flat Plate Junction Flow, Volumes 1 and 2," DTNSRDC Reports 86/051 and 86/052 (Dec 1986).
2. Kwak, D., J.L.C. Chang, S.P. Shanks, and S.R. Chakravarthy, "A Three-Dimensional Incompressible Navier-Stokes Flow Solver Using Primitive Variables," *AIAA Journal* Vol. 24, pp. 390-396 (1986).
3. Chorin, A.J., "A Numerical Method for Solving Incompressible Viscous Flow Problems," *Journal of Computational Physics*, Vol. 2, pp. 12-26 (1967).
4. Sorenson, R.L., "A Computer Program to Generate Two-Dimensional Grids about Airfoils and Other Shapes by the Use of Poisson's Equation," NASA Technical Memorandum 81198 (1980).
5. Baldwin, B.S. and H. Lomax, "Thin Layer Approximation and Algebraic Model for Separated Turbulent Flows," AIAA Paper 78-257, Huntsville, AL (Jan 1978).
6. Mehta, U., K.C. Chang, and T. Cebeci, "A Comparison of Interactive Boundary Layer and Thin-Layer Navier-Stokes Procedures," *Numerical and Physical Aspects of Aerodynamic Flows III*, ed. T. Cebeci, Springer-Verlag (1986).
7. Hung, C. and P.G. Buning, "Simulation of Blunt-fin-induced Shock-wave and Turbulent Boundary-Layer Interaction," *J. Fluid Mech.*, Vol. 154, pp. 163-185 (1985).
8. Buning, P.G. and J.L. Steger, "Graphics and Flow Visualization in Computational Fluid Dynamics," *Proceedings of the AIAA 7th Computational Fluid Dynamics Conference*, Cincinnati, Ohio (1985).
9. Devenport, W.J. and R.L. Simpson, "Some Time Dependent Features of Turbulent Appendage-Body Flows," 16th Symposium on Naval Hydrodynamics, 14-18 Jul 1986, Berkeley, CA.
10. Shabaka, I.M.M.A. and P. Bradshaw, "Turbulent Flow Measurements in an Idealized Wing/Body Junction," *AIAA Journal*, Vol. 19, No. 2 (1981).
11. Bradshaw, P., T. Cebeci, and J. Whitelaw, *Engineering Calculation Methods for Turbulent Flows*, Academic Press, New York, p. 321 (1981).
12. Kaynak, U., PhD Thesis, "Computation of Transonic Wing Separated Flow Using an Euler/Navier-Stokes Zonal Approach," Aeronautics Dept., Stanford University (Dec 1985).
13. Visbal, M. and D. Knight, "The Baldwin-Lomax Turbulence Model for Two-Dimensional Shock-Wave/Boundary-Layer Interactions," *AIAA Journal*, Vol. 22, pp. 921-928 (Jul 1984).

INITIAL DISTRIBUTION

Copies

1 DARPA/Wisniewski
 3 ONR
 1 1132F (Reichman)
 1 1132F (Whitehead)
 1 1245 (Hansen)
 1 ONR/Boston
 1 ONR/Chicago
 1 ONR/New York
 1 ONR/Pasadena
 1 ONR/San Francisco
 2 NRL
 1 Code 2027
 1 Code 2629
 3 USNA
 1 Tech Lib
 1 Nav Sys Eng Dept
 1 B. Johnson
 1 NAVPGSCOL/Lib
 1 NOSC/Lib
 1 NCSC/712
 1 NCEL/131
 1 NSWC, White Oak/Lib
 1 NSWC, Dahlgren/Lib
 1 NUSC/Lib

Copies

3 NAVSEA
 1 SEA 55W3 (E. Comstock)
 1 SEA 55W31 (G. Jones)
 1 SEA 55W33 (W. Sandburg)
 1 NAVFAC/032
 1 NADC
 12 DTIC
 1 AFOSR/NAM
 2 MARAD
 1 Div of Ship R&D
 1 Lib
 1 NASA/HQ/Lib
 3 NASA/Ames Res Ctr
 1 D. Kwak
 1 J.L. Steger
 1 Lib
 3 NASA/Langley Res Ctr
 1 Lib
 1 D. Bushnell
 1 Rubendran
 1 NBS/Lib
 1 LC/Sci & Tech
 2 Brown University
 1 Sirovich
 1 Lib
 3 U of Cal, Berkeley/Dept Naval Arch
 1 Lib
 1 W. Webster
 1 R. Yeung

Copies

- 2 U of Cal, San Diego
 - 1 H. Abarbanel
 - 1 Scripps Inst Lib
- 1 U of Cal, Santa Barbara/Tulin
- 2 CIT
 - 1 Aero Lib
 - 1 A.J. Acosta
- 1 California State Univ, Long Beach
Cebeci
- 1 Catholic U of Amer/Civil & Mech Eng
- 1 Cornell U/Shen
- 1 Georgia Inst of Tech/McMahon
- 1 Harvard U/Gordon McKay Lib
- 3 U of Iowa
 - 1 Lib
 - 1 V.C. Patel
 - 1 C.J. Chen
- 4 MIT
 - 1 Lib
 - 1 J.R. Kerwin
 - 1 T.F. Olgilvie
 - 1 J.N. Newman
- 2 U of Minn, St. Anthony Falls
 - 1 Lib
 - 1 Arndt
- 1 U of Mich/NAME/Lib
- 3 Penn State
 - 1 C.L. Merkle
 - 1 R.E. Henderson
 - 1 ARL Lib

Copies

- 2 Princeton U
 - 1 Orszag
 - 1 Lib
- 1 U of Rhode Island/F.M. White
- 2 SIT
 - 1 McKee
 - 1 Lib
- 1 U of Southern California/Ho
- 1 Stanford U/Eng Lib
- 1 U of Virginia/Aero Eng Dept
- 3 VPI
 - 1 Pierce
 - 1 Schetz
 - 1 Simpson
- 2 Webb Inst
 - 1 Lib
 - 1 Ward
- 1 SNAME/Tech Lib
- 1 Bell Aerospace
- 1 National Science Foundation/
Eng Div Lib
- 2 Boeing Company, Seattle
 - 1 Marine System
 - 1 P. Rubbert
- 1 Bolt, Beranek & Newman/Lib
- 1 General Dynamics, EB/Boatwright
- 2 Flow Research
 - 1 Wen-Huei Joh
 - 1 Duncan
- 1 Gibbs & Cox/Tech Info

Copies

CENTER DISTRIBUTION

		Copies	Code	Name
2	Gould Defense System, Inc			
	1 Meng			
	1 Dickinson	1	012.2	Nakonechny
1	Grumman Aerospace Corp/Lib	1	15	Morgan
		1	1504	Monacella
1	Tracor Hydronautics/Lib	1	152	Lin
		1	1522	Sung
1	Lockheed, Sunnyvale/Waid	1	154	McCarthy
		1	1542	Huang
1	Lockheed, Georgia Co /Lib	10	1542	Hendrix
		1	1543	Rood
1	Lockheed Missile and Space Co/Burke	1	1543	Anthony
		1	1544	Peterson
2	McDonnell Douglas, Long Beach	1	1544	Reed
	1 T. Cebeci			
	1 J.L. Hess	1	1843	Hausssling
1	Newport News Shipbuilding/Lib	10	5211.1	Reports Control
		1	522.1	TIC (C)
1	Nielsen Eng & Research	1	522.2	TIC (A)
1	Northrop Corp/Aircraft Div			
1	Rockwell International/Rocketdyne Div/ Chang			
1	TRW Systems Group/Lib			
1	United Technology/East Hartford, Conn			
1	Westinghouse Electric/Lib			

DTNSRDC ISSUES THREE TYPES OF REPORTS:

- 1 **DTNSRDC reports, a formal series**, contain information of permanent technical value. They carry a consecutive numerical identification regardless of their classification or the originating department.
- 2 **Departmental reports, a semiformal series**, contain information of a preliminary, temporary, or proprietary nature or of limited interest or significance. They carry a departmental alphanumerical identification.
- 3 **Technical memoranda, an informal series**, contain technical documentation of limited use and interest. They are primarily working papers intended for internal use. They carry an identifying number which indicates their type and the numerical code of the originating department. Any distribution outside DTNSRDC must be approved by the head of the originating department on a case-by-case basis.

END

DATE

FILMED

DEC.

1987